Research Square

Preprints are preliminary reports that have not undergone peer review.
They should not be considered conclusive, used to inform clinical practice,
or referenced by the media as validated information.

Enhanced β-decay rates and the role of underlying nuclear structure at the neutron drip line

Tawfik Gaballah

tg1250@msstate.edu

Mississippi State University https://orcid.org/0009-0003-2846-5117

Benjamin Crider

Mississippi State University https://orcid.org/0000-0001-7153-8762

Heather L. Crawford

Lawrence Berkeley National Laboratory https://orcid.org/0000-0002-7765-4235

Sean Liddick

Michigan State University https://orcid.org/0000-0003-1589-891X

Sota Yoshida

Utsunomiya University

James Allmond

Oak Ridge National Laboratory https://orcid.org/0000-0001-6533-8721

Robert Grzywacz

University of Tennessee https://orcid.org/0000-0002-0920-2587

Vandana Tripathi

Florida State University https://orcid.org/0000-0002-8850-1357

Yutaka Utsuno

Japan Atomic Energy Agency https://orcid.org/0000-0001-5404-7320

Corrigan Appleton

Lawrence Berkeley National Laboratory

Evan Argo

Facility for Rare Isotope Beams

Honey Arora

Institute for Basic Science

Peter Bender

University of Massachusetts, Lowell

Jessica Berkman

Michigan State University https://orcid.org/0009-0001-9753-0096

Soumik Bhattacharya

Variable Energy Cyclotron Centre

Nico Braukman

Universtity of Tennessee, Knoxville https://orcid.org/0009-0000-4666-0440

Christopher Campbell
Lawrence Berkeley National Laboratory https://orcid.org/0000-0003-3577-4316

Aaron Chester
Michigan State University

James Christie
University of Tennessee, Knoxville

Benjamin Clark
Facility for Rare Isotope Beams

Roderick Clark
Lawrence Berkeley National Laboratory

Ian Cox
University of Tennessee, Knoxville https://orcid.org/0000-0002-6807-3658

Amelia Doetsch
Facility for Rare Isotope Beams

Jeremias Garcia-Duarte
Lawrence Livermore National Laboratory https://orcid.org/0000-0002-8781-3834

Paul Fallon
Lawrence Berkeley National Laboratory https://orcid.org/0009-0004-2687-2496

Tim Gray
University of Tennessee, Knoxville https://orcid.org/0000-0003-3965-6130

Jason Harke
Lawrence Livermore National Laboratory

Rahul Jain
Lawrence Livermore National Laboratory https://orcid.org/0000-0001-9859-1512

Thomas King
Oak Ridge National Laboratory https://orcid.org/0000-0003-0649-3275

Noritaka Kitamura
The University of Tokyo

Filip Kondev
Argonne National Laboratory https://orcid.org/0000-0002-9567-5785

Alex Laminack
Oak Ridge National Laboratory https://orcid.org/0000-0002-5166-4523

Brenden Longfellow
Argonne National Laboratory

Rebeka Lubna
Facility for Rare Isotope Beams

Miguel Madurga
University of Tennessee, Knoxville

Ruchi Mahajan
University of Kentucky
Mejdi Mogannam
Air Force Institute of Technology
Timilehin Ogunbeku
Lawrence Livermore National Laboratory
Weijia Ong
Lawrence Livermore National Laboratory
Carlotta Porzio
CERN-ISOLDE
Eleanor Ronning
Istituto Nazionale di Fisica Nucleare
Krzysztof Rykaczewski
Oak Ridge National Laboratory https://orcid.org/0000-0002-5717-3418
Dustin Scriven
Facility for Rare Isotope Beams https://orcid.org/0000-0002-3853-2200
Darek Seweryniak
Argonne National Lab https://orcid.org/0009-0003-3028-9693
Artemis Spyrou
Michigan State University https://orcid.org/0000-0002-8642-8352
Sam Tabor
Florida State University
Tyler Wheeler
Facility for Rare Isotope Beams
Mathis Wiedeking
Lawrence Berkeley National Laboratory https://orcid.org/0000-0003-4983-3882
Jeff Winger
Mississippi State university
Yiyi Zhu
TRIUMF

Physical Sciences - Article

Keywords:

Posted Date: November 24th, 2026

DOI: https://doi.org/10.21203/rs.3.rs-11570096/v1

License: This work is licensed under a Creative Commons Attribution 4.0 International License.
Read Full License

Additional Declarations: There is **NO** Competing Interest.

Enhanced β-decay rates and the role of underlying nuclear structure at the neutron drip line

T. Gaballah[1,2*], B. P. Crider[1], H. L. Crawford[3], S. N. Liddick[2,4], S. Yoshida[5,6], J. M. Allmond[7], R. Grzywacz[8], V. Tripathi[9], Y. Utsuno[10,11], C. J. Appleton[3], E. Argo[2,12], H. Arora[13,18], P. C. Bender[14], J. M. Berkman[2,4], S. Bhattacharya[9,15], N. Braukman[8], C. M. Campbell[3], A. Chester[2], J. M. Christie[7,8], B. R. Clark[1,19], R. M. Clark[3,†], I. Cox[8,20], A. Doetsch[2,12], J. G. Duarte[16], P. Fallon[3], T. J. Gray[7,8], J. T. Harke[16], R. Jain[2,21], T. T. King[7], N. Kitamura[8,22], F. G. Kondev[17], A. Laminack[7], B. Longfellow[16,17], R. S. Lubna[2], M. Madurga[8], R. Mahajan[2,23], M. J. Mogannam[2,4,24], T. H. Ogunbeku[1,2], W. J. Ong[16], C. Porzio[3,25], E. K. Ronning[2,4,26], K. P. Rykaczewski[7], D. P. Scriven[2], D. Seweryniak[17], A. Spyrou[2,12], S. L. Tabor[9], T. Wheeler[2,12], M. Wiedeking[3], J. A. Winger[1], Y. Zhu[14,27]

[1*] Department of Physics and Astronomy, Mississippi State University, Mississippi State, MS, 39762, USA.

[2] Facility for Rare Isotope Beams, Michigan State University, East Lansing, MI, 48824, USA.

[3] Nuclear Science Division, Lawrence Berkeley National Laboratory, Berkeley, CA, 94720, USA.

[4] Department of Chemistry, Michigan State University, East Lansing, MI, 48824, USA.

[5] School of Data Science and Management, Utsunomiya University, Utsunomiya, 321-8505, Japan.

[6] RIKEN Nishina Center for Accelerator-based Science, RIKEN, Wako, 351-0198, Japan.

[†] Deceased: R. M. Clark.

[7] Physics Division, Oak Ridge National Laboratory, Oak Ridge, TN, 37831, USA.
[8] Department of Physics and Astronomy, University of Tennessee, Knoxville, TN, 37996, USA.
[9] Department of Physics, Florida State University, Tallahassee, FL, 32306, USA.
[10] Advanced Science Research Center, Japan Atomic Energy Agency, Tokai, Ibaraki, 319-1195, Japan.
[11] Center for Nuclear Study, The University of Tokyo, 7-3-1 Hongo, Bunkyo, Tokyo, 113-0033, Japan.
[12] Department of Physics and Astronomy, Michigan State University, East Lansing, MI, 48824, USA.
[13] Department of Physics, Central Michigan University, Mount Pleasant, MI, 48859, USA.
[14] Department of Physics and Applied Physics, University of Massachusetts Lowell, Lowell, MA, 01854, USA.
[15] Variable Energy Cyclotron Centre, Kolkata, 700064, India.
[16] Lawrence Livermore National Laboratory, Livermore, CA, 94550, USA.
[17] Argonne National Laboratory, Lemont, IL, 60439, USA.
[18] Present address: Center for Exotic Nuclear Studies, Institute for Basic Science, Daejeon, 34126, Republic of Korea.
[19] Present address: Facility for Rare Isotope Beams, Michigan State University, East Lansing, MI, 48824, USA.
[20] Present address: Argonne National Laboratory, Lemont, IL, 60439, USA.
[21] Present address: Lawrence Livermore National Laboratory, Livermore, CA, 94550, USA.
[22] Present address: The University of Tokyo, Tokyo, 113-0033, Japan.
[23] Present address: Department of Physics and Astronomy, University of Kentucky, Lexington, Kentucky, 40506-0055, USA.
[24] Present address: Air Force Institute of Technology, Dayton, Ohio, 45433, USA.
[25] Present address: CERN-ISOLDE, 1211 Geneva 23, Switzerland.
[26] Present address: Istituto Nazionale di Fisica Nucleare, Sezione di Padova, Padua, 35131, Italy.
[27] Present address: TRIUMF, 4004 Wesbrook Mall, Vancouver, British Columbia, V6T 2A3, Canada.

*Corresponding author(s). E-mail(s): tawfikgaballah@gmail.com;

Abstract

Nuclei are bound collections of protons and neutrons whose stability reflects a delicate balance of the forces inside matter. When many extra neutrons are added, this balance shifts: traditional arrangements can reorganize, allowing new shapes to compete and previously high-energy configurations to emerge at low energies. Measurements at the limits of nuclear binding are scarce but essential for testing descriptions of this evolution. How far toward these neutron-rich limits does nuclear structure continue to influence β-decay half-lives, even as the decay energy becomes very large? Here we report the first β-decay half-life measurements of ^{31}F and ^{37}Na, nuclei at or near the neutron-rich limits of binding. The measured half-lives of $\mathbf{1.31^{+0.25}_{-0.21}}$ ms for ^{31}F and $\mathbf{1.65^{+0.33}_{-0.27}}$ ms for ^{37}Na are the two shortest directly measured β^--decay half-lives by central value, with ^{31}F the shortest. Large-scale shell-model calculations indicate that these rapid decays depend not only on the large energy available for decay but also on shell evolution that places accessible transition strength at lower daughter excitation energies, where phase space remains large. These measurements replace extrapolated lifetimes with experimental benchmarks and show that, even at the neutron-rich limits of binding, exceptionally rapid β decays retain sensitivity to internal nuclear structure.

The quest to delineate the boundaries of nuclear stability stands as a cornerstone of contemporary nuclear physics[1,2]. Venturing into regions far from the valley of β stability, where the neutron-to-proton ratio is optimal for nuclear binding, reveals phenomena that challenge traditional shell-model predictions[3]. In the territories of the nuclear chart at the extremes of neutron excess, the addition of even a single neutron may no longer result in a bound nucleus, defining the neutron drip line[4]. Exploring these boundaries is essential for providing insights into the forces that govern nuclear matter.

Far from stability (Fig. 1a), nuclei exhibit pronounced changes in shell structure, departing from the traditional spherical shell-model picture with shell closures at the magic numbers 2, 8, 20, 28, 50, 82, and (for neutrons) 126[5]. These numbers correspond to large energy separations between groups of single-particle states, such that completely filling the levels up to one of these gaps imparts additional stability—much like the noble gases achieve chemical stability upon filling an electron shell. Away from stability, it is well established that there is an evolution of single-particle states

which depends on the neutron-to-proton ratio[6] and results in the disappearance of traditional spherical shell gaps and the appearance of new subshell gaps[7], altering the shell-model description. Beyond this, near the limits of binding, the energy required to remove the least-bound neutron (the neutron separation energy) can become comparable to the strength of neutron pairing correlations (the pairing gap)[8,9]. Under such conditions, which are plausibly relevant for ^{31}F[10] and possibly for ^{37}Na[11], the mean-field picture of localized single-particle states begins to blur, and the nucleus approaches the behavior of an open quantum system. This opens the possibility of further modifications to shell structure and the formation of features such as neutron skins or halos[12].

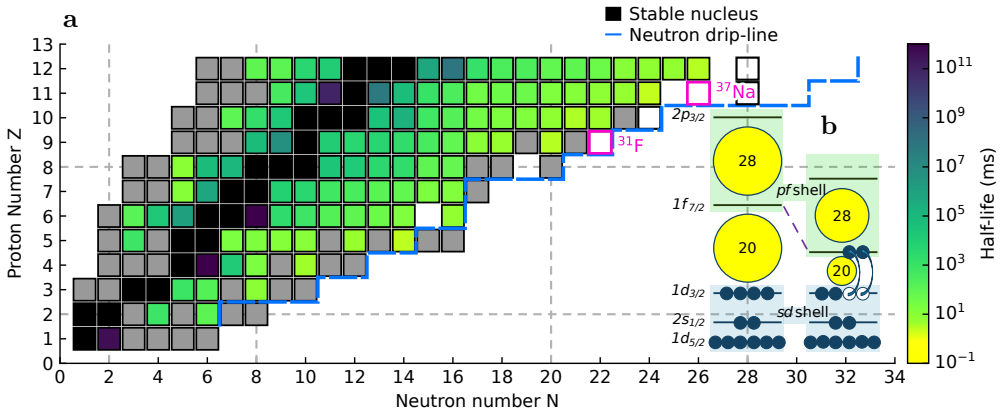

Fig. 1 Nuclear landscapes at the neutron drip line. a, Evaluated β-decay half-lives across the chart of nuclides[13]. Grey cells indicate nuclides for which β-decay is not the primary decay mode. ^{31}F and ^{37}Na, located at or near the neutron drip line as predicted by Ref. [14], are marked. **b,** Schematic description of normal and intruder configurations near the $N = 20$ island of inversion[15]. Far from stability, the reduced $N = 20$ shell gap permits neutron pairs to be promoted from the *sd* shell to the *pf* shell so that deformed intruder configurations dominate the level structure, leading to lowered first-excited-state energies and significant structural changes. Panel b is schematic and does not share the neutron- and proton-number coordinates of panel a.

The neutron-rich isotopes ^{31}F and ^{37}Na occupy key positions along the boundary of nuclear binding where shell evolution, deformation, and weak binding converge[2]. Both lie in regions where conventional magic numbers weaken and intruder configurations, formed by promoting nucleons across a shell gap into higher-lying orbitals (Fig. 1b),

can compete with normal configurations for the ground state[15], providing sensitive probes of nuclear structure near the neutron drip line.

The isotope ^{31}F ($Z = 9$, $N = 22$) is the heaviest confirmed bound fluorine isotope[13] and defines the fluorine drip line[16]. Earlier theoretical studies placed the fluorine drip line at lighter isotopes (around ^{29}F) and suggested that heavier fluorine isotopes might undergo prompt neutron emission rather than β decay[17,18]. The observation of the bound ^{31}F[19] extended the fluorine chain drip line and placed an additional fluorine isotope at the edge of the $N = 20$ "island of inversion", where cross-shell neutron excitations into the pf shell and associated deformation play a dominant role in the Ne–Na–Mg region[20] (Fig. 1).

For sodium, the isotope ^{37}Na ($Z = 11$, $N = 26$) was first observed in 2002 in fragmentation experiments at RIKEN and GANIL[21,22], establishing one of the most neutron-rich sodium nuclides known at the time. More recently, ^{39}Na was identified as particle-stable, extending the (known) sodium chain farther into the neutron-rich region[23]. Although ^{37}Na lies beyond the canonical $N = 20$ closure, it resides within the extended domain where the island-of-inversion phenomenology persists for light Z, with the weakening of the $N = 20$ gap and the participation of neutron pf-shell intruders leading to deformed ground states between $N = 20$ and $N = 28$ in the Ne–Na–Mg chains[20].

In this regime of weak binding and altered shell ordering, precise experimental information is needed to provide stringent constraints on the balance between intruder and normal configurations and the possible impacts of weak binding. Before the present work, no experimental β-decay half-life measurements had been reported for either ^{31}F or ^{37}Na. The Present measurements provide key benchmarks at the far neutron-rich edge of nuclear binding.

At the limits of stability, experimental access to nuclear structure information becomes increasingly difficult: lifetimes are short, production yields are low, and direct

detailed spectroscopy becomes challenging. Yet these systems hold the key to understanding how nuclear forces evolve as binding energies vanish. In such cases, β decay serves as a uniquely sensitive probe, providing valuable information at low beam production rates. While detailed spectroscopy, which can uncover level structures and provide direct insight into shell evolution, is not possible at the lowest rates, β-decay half-lives can provide a critical first piece of information[24]. This integral quantity depends on both the energy available for decay, expressed by the decay Q value (Q_β), and the nuclear structure that determines the accessible transition strength[25,26].

This raises a fundamental question near the neutron drip line: why does a larger ground-state to ground-state β-decay energy not necessarily imply a shorter half-life, and does nuclear structure still govern the fastest decays? As the ratio of neutrons to protons increases, Q_β generally increases, and decay energies near the drip line can reach values of order 20–30 MeV[27]. For allowed transitions, the phase space available to the emitted electron and antineutrino increases rapidly with the energy released in the decay, scaling approximately as $(Q_\beta - E_x)^5$, where E_x is the excitation energy of the populated state in the daughter nucleus[25]. From energetics alone, one might therefore expect the half-life to become progressively shorter with increasing neutron excess, with little sensitivity to other influencing factors. Whether that expectation holds depends on how the transition strength is distributed among the accessible daughter states.

Two structural effects can counter this expectation. First, the separation of neutron and proton Fermi surfaces, together with the orbital occupations, can affect the Gamow–Teller (GT) strength available to low-lying states in the daughter nucleus[9]. In a single-particle picture, GT transitions predominantly convert a neutron into a proton in an orbital with the same spatial quantum numbers (n, l). Depending on the orbital energies and occupations, the corresponding proton orbital can lie well

above the proton Fermi surface, reducing the strength available to low-energy daughter states. Second, collective correlations can concentrate a substantial fraction of the GT strength in a giant resonance at higher excitation energies, where individual transitions receive less phase-space enhancement[28]. More generally, large Q_β values can drive nuclei into the millisecond regime but do not by themselves imply a universal limiting half-life near 1 ms: the distribution of accessible transition strength determines how effectively the available phase space is used. Comparisons among nuclei with similar Q_β values can probe the role of structure in producing exceptionally rapid decays.

Here we present the first experimental measurements of the β^--decay half-lives of ^{31}F and ^{37}Na, providing new constraints on theoretical descriptions of intruder-dominated structure near the neutron drip line. By central value, these are the two shortest directly measured nuclear β^--decay half-lives in our updated experimental compilation, with ^{31}F the shortest. Extended Data Table 1 places the measurements among the ten shortest β-decay half-lives compiled from evaluated data and subsequent measurements. This comparison spans very neutron-rich nuclei from boron to titanium, extending beyond the $N = 20$ island of inversion. By comparing these measurements with large-scale shell-model calculations and nuclei with similar Q_β values, we examine how the distribution of accessible transition strength shapes these exceptionally rapid decays. These measurements were made possible at the Facility for Rare Isotope Beams (FRIB) by the FRIB Decay Station Initiator (FDSi)[29,30], building upon the success of FRIB's inaugural user experiment[24].

Results

Here we present the first experimental measurements of the β-decay half-lives of ^{31}F and ^{37}Na. Given the limited statistics and the multiple correlated parameters entering the decay-curve fits, the analysis began with a Bayesian framework designed to test

the stability of the inferred half-lives against variations in background and β-delayed neutron branching ratios. The posterior medians and central 68% credible intervals gave half-lives of $1.31^{+0.25}_{-0.21}$ ms for ^{31}F and $1.65^{+0.33}_{-0.27}$ ms for ^{37}Na (Fig. 2b,c). Posterior correlations in both cases show that the parent half-life is essentially insensitive to the individual neutron-emission probabilities, with only a modest dependence on the total neutron-emission probability, and is more strongly correlated with the initial activity (Extended Data Figs. 1 and 2; Methods). As a validation of the analysis, the previously known ^{35}Na half-life was extracted from the present data using the same procedure, yielding 2.47(9) ms, consistent with the earlier FRIB measurement[24] and supporting the robustness of the analysis in the low-statistics regime.

As a cross-check using a different analysis procedure, frequentist maximum-likelihood Bateman fits fixed the β-delayed x-neutron-emission probabilities, P_{xn}, to values from the finite-range droplet model plus quasiparticle random-phase approximation (FRDM+QRPA)[31]. The resulting half-lives, 1.45 ± 0.22 ms for ^{31}F and 1.58 ± 0.25 ms for ^{37}Na, are statistically consistent with the Bayesian results.

Extended Data Fig. 3 compares the Bayesian and frequentist results. The corresponding posterior distributions and correlations are shown in Extended Data Figs. 1 and 2, with numerical summaries in Extended Data Table 2.

Discussion

Large Q_β values near the neutron drip line provide enough phase space to drive β-decay half-lives into the millisecond regime, but do not uniquely determine the rate. The rate also depends on where Gamow–Teller (GT) and first-forbidden (FF) strength is distributed within the decay window. The present measurements therefore test whether sensitivity to nuclear structure survives at extreme decay energies.

As a global baseline, we compare our measurements with the JAEA Gross-theory predictions calculated using KTUY mass-model Q_β values[33]. Gross theory combines

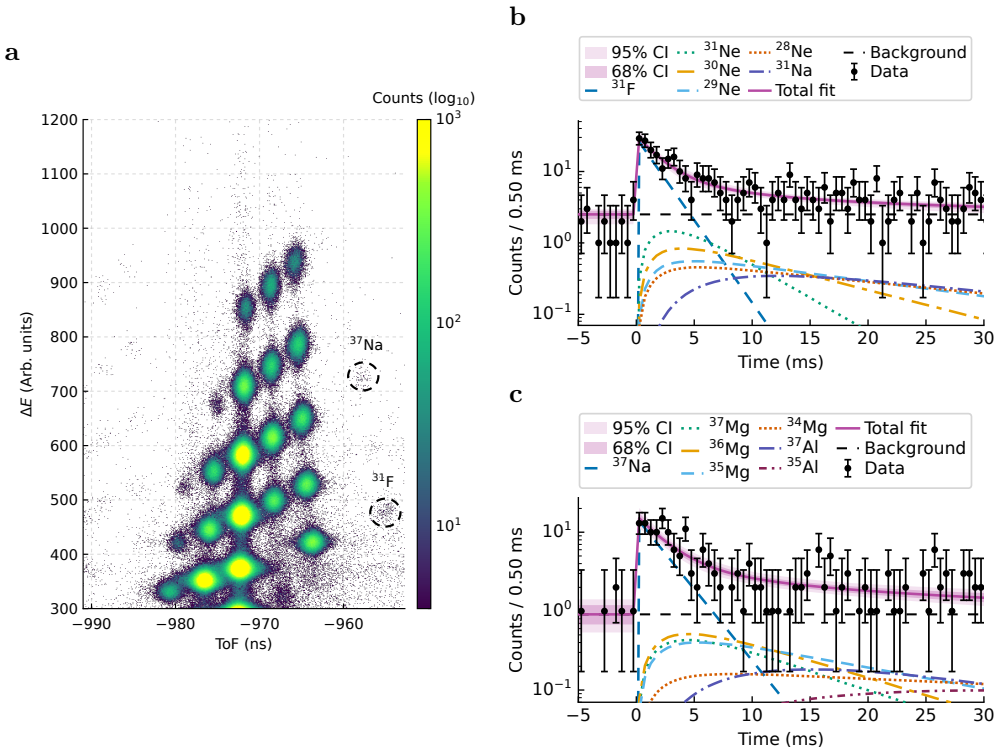

Fig. 2 Particle identification and decay-curve fits. a, Particle-identification spectrum for ions implanted in the YSO detector in the ^{37}Na setting. Bayesian fits using the Bateman decay-chain model for ^{31}F (**b**; 197 implanted ions) and ^{37}Na (**c**; 99 implanted ions). Solid curves are the total posterior-median fits. The individual decay-chain contributions include the parent and the $\beta 0n$, $\beta 1n$, $\beta 2n$, and $\beta 3n$ daughters, together with the relevant granddaughters: ^{31}Na for ^{31}F, and ^{37}Al and ^{35}Al for ^{37}Na. Shaded regions indicate the pointwise central 68% and 95% posterior credible intervals for the total fitted curve, and dashed black lines show background constrained by the reverse-time correlation.

decay energetics with an averaged transition-strength distribution[25], so it provides a statistical baseline rather than a calculation based on Q_β alone. The tabulated predictions of 1.563 ms for ^{31}F and 1.318 ms for ^{37}Na reproduce the millisecond scale of the measurements.

The global FRDM+QRPA calculation[31] also reproduces the millisecond half-life scale of ^{31}F and ^{37}Na (Fig. 3), but its agreement across the F and Na isotopic chains is not robust. In the Na chain, it underpredicts the half-lives of the lighter isotopes and produces an odd–even staggering that is not evident in the experimental data. A similar overprediction of the odd–even staggering was reported for the

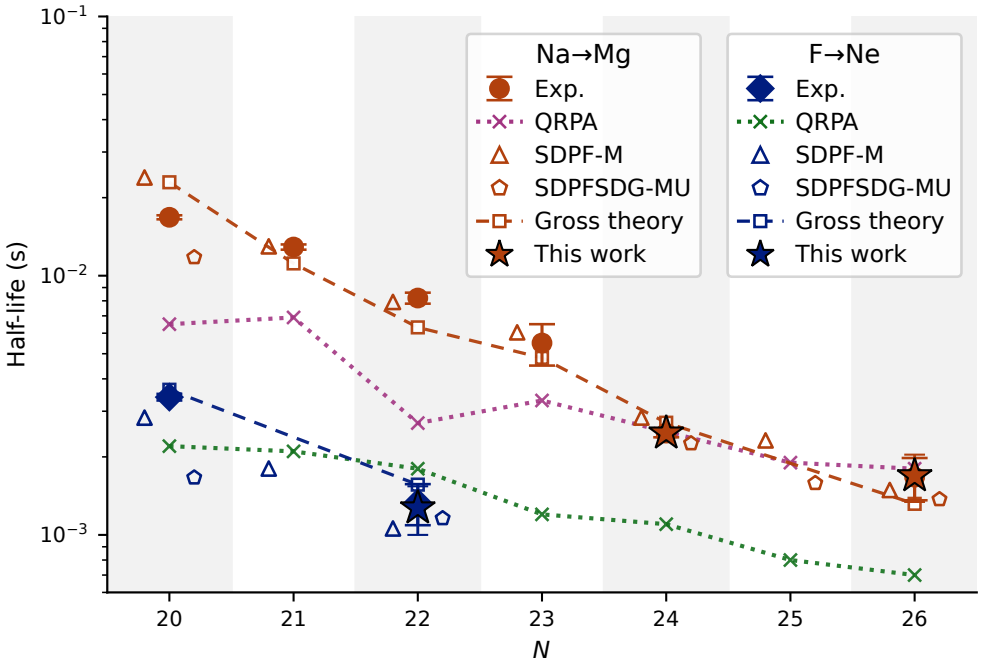

Fig. 3 Measured half-lives and theoretical comparisons. Experimental F and Na half-lives are compared with FRDM+QRPA, Gross-theory and SDPF-M/SDPFSDG-MU shell-model predictions. Stars mark the first measurements of ^{31}F and ^{37}Na and the ^{35}Na validation measurement. Other experimental values are from NUBASE2020[32] and Ref.[24]. Shell-model predictions use adopted mass-evaluation Q_β values; Gross-theory predictions (long-dashed lines with open squares) use KTUY mass-model values[33]. All theoretical half-lives describe β decay only and exclude competing particle-decay widths. Calculations using shell-model Q_β values and alternative ground-state spin-parity assignments are shown in Extended Data Fig. 4.

neighboring Mg–P isotopic chains in the first FRIB measurement[24]. Agreement with the ^{29}F measurement is also poor. Both global approaches combine decay energetics with model-dependent transition-strength distributions. Their agreement with the observed millisecond scale therefore does not, by itself, establish that the detailed nuclear structure is reproduced.

To test this structure dependence, we performed large-scale shell-model calculations with the SDPF-M interaction[34] and the SDPFSDG-MU interaction[26,35], the latter being an extension of SDPF-MU[36] into the $sd+pf+sdg$ valence space. SDPF-M was used to describe intruder-dominated configurations near the $N = 20$ island of inversion, including the $2\hbar\omega$ calculation adopted for ^{31}F. SDPFSDG-MU was used

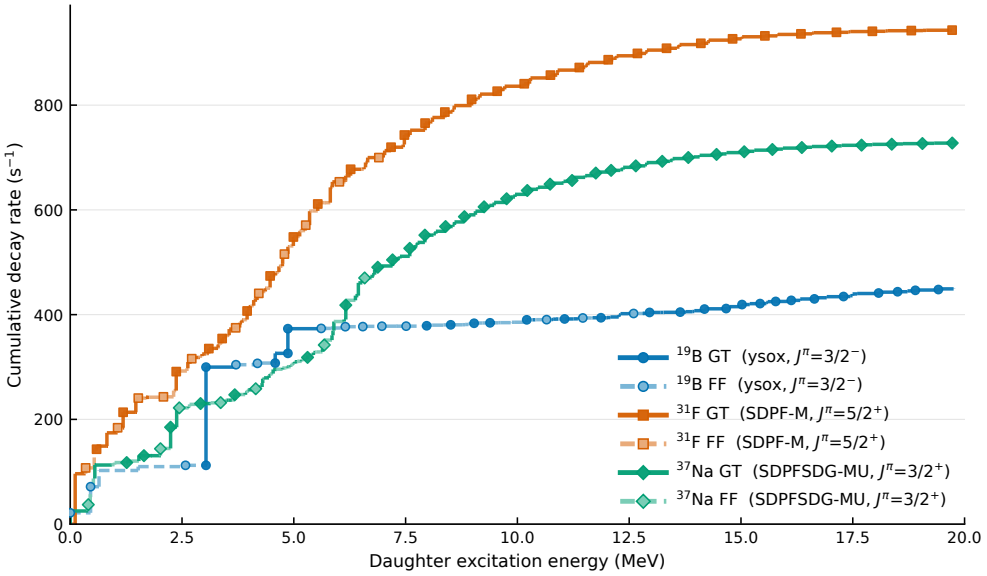

Fig. 4 Cumulative calculated inverse half-lives reveal structure-dependent decay pathways. Cumulative inverse half-lives, including both Gamow–Teller (GT) and first-forbidden (FF) transitions, are shown as a function of daughter excitation energy for ^{19}B, ^{31}F and ^{37}Na, calculated using the YSOX[37], SDPF-M[34] and SDPFSDG-MU[26,35] interactions, respectively. The calculations used adopted mass-evaluation Q_β values[27]. Darker and lighter segments indicate GT and FF contributions, respectively, within each cumulative GT+FF curve. The few dominant branches in ^{19}B contrast with the broader distribution of decay strength across low- and intermediate-energy daughter states in ^{31}F and ^{37}Na. A steep rise toward the final cumulative rate at low daughter excitation energy indicates that a significant fraction of the decay rate is accumulated while the available β endpoint energy, $Q_\beta - E_x$, remains large.

for the more neutron-rich Na–Mg systems with $N \geq 24$, including ^{37}Na. Alternative parent spin–parity assignments were considered where the experimental ground-state assignment is not uniquely established. For the structure-dependent comparisons discussed below, we also used a YSOX calculation[37] for ^{19}B, which serves as a point of comparison. Both allowed Gamow–Teller (GT) and first-forbidden (FF) transitions were included in the half-life predictions and cumulative decay distributions. The GT matrix elements were evaluated with quenching factors $q_{\mathrm{GT}} = 0.74$ for SDPFSDG-MU and $q_{\mathrm{GT}} = 0.60$ for SDPF-M and YSOX. These factors multiply the GT operator, so the corresponding $B(\mathrm{GT})$ strengths scale as q^2_{GT}. The FF contributions were calculated using the effective operators described in Refs.[26,35]. The total half-life was

obtained by summing the inverse partial half-lives,

$$\frac{1}{T_{1/2}} = \sum_{f\in \mathrm{GT}} \frac{1}{t_{i\to f}^{\mathrm{GT}}} + \sum_{f\in \mathrm{FF}} \frac{1}{t_{i\to f}^{\mathrm{FF}}}, \tag{1}$$

where both sums include all daughter states within the corresponding decay window. FF transitions account for approximately 30%, 15%, and 10% of the calculated decay rates for ^{19}B, ^{31}F, and ^{37}Na, respectively, with GT transitions providing the dominant contribution in all three cases. Further details are provided in the Methods subsection "Detailed shell-model calculations".

The cumulative GT+FF contributions in Fig. 4 illustrate how the excitation-energy distribution of accessible transition strength affects the decay rate. Although the adopted Q_β value for ^{19}B is slightly larger than the estimated value for ^{31}F, its measured half-life of 2.92(13) ms[27,38] is roughly twice as long. The calculated ^{19}B rate is dominated by a few strong branches, whereas in ^{31}F appreciable transition strength is distributed among a larger set of low-lying ^{31}Ne states, with additional contributions at intermediate excitation energies. Because these states retain large endpoint energies, $Q_\beta - E_x$, even transitions with moderate decay strengths can contribute appreciably through the steep energy dependence of the β-decay phase space. For allowed GT transitions, the leading dependence is approximately $(Q_\beta - E_x)^5$, whereas FF rates include additional energy- and momentum-dependent shape factors. The calculated rate difference ,therefore, strongly reflects where appreciable transition strength is placed within the decay window, rather than the size of the decay window or the daughter level density alone.

For ^{31}F, the reduced $N = 20$ shell gap associated with shell evolution in the island-of-inversion region lowers the excitation-energy scale of GT-accessible configurations in ^{31}Ne. This provides a microscopic origin for the favorable low-energy distribution of transition strength shown in Fig. 4: the shell-gap evolution and the calculated strength

distribution are therefore complementary descriptions of the same underlying physics. The half-life is sensitive to this relative parent–daughter structure but does not, by itself, determine the magnitude of the explicit intruder admixture in the ^{31}F parent wave function.

For ^{37}Na, the calculation likewise places appreciable accessible strength across low and intermediate daughter excitation energies. The more detailed microscopic origin is less constrained, however, because fewer theoretical studies of the ^{37}Na ground-state structure and spin-parity are available. We therefore do not assign the ^{37}Na result to a specific shell-gap mechanism. In neither nucleus can the half-life alone uniquely determine the parent spin, parity, or wave-function composition. The measurements are nevertheless consistent with exceptionally rapid β-decay rates retaining sensitivity to shell evolution near the limits of binding.

Shell evolution at the edge of stability

We have reported the first experimental β-decay half-life measurements of the neutron-rich drip-line nucleus ^{31}F and the near-drip-line nucleus ^{37}Na. The extracted values, $T_{1/2} = 1.31^{+0.25}_{-0.21}$ ms for ^{31}F and $T_{1/2} = 1.65^{+0.33}_{-0.27}$ ms for ^{37}Na from the Bayesian analysis, are, by central value, the two shortest directly measured nuclear β^--decay half-lives in our updated experimental compilation, with ^{31}F the shortest (Extended Data Table 1).

These measurements were made possible by implantation-decay correlations at FRIB in a regime where only 197 ^{31}F and 99 ^{37}Na ions were observed. Both the JAEA Gross-theory predictions and the global FRDM+QRPA calculations reproduce the observed millisecond scale. The close Gross-theory agreement indicates that bulk decay energetics and an averaged strength distribution are sufficient to reproduce the overall millisecond scale, but do not identify the microscopic origin of the transition strength responsible for that rate.

Large-scale shell-model calculations however show that the rapid decay of ^{31}F and ^{37}Na is shaped by the placement of accessible transition strength at low and intermediate daughter excitation energies. For ^{31}F, the calculations connect this favorable strength distribution to shell evolution associated with the reduced $N = 20$ gap at the edge of the island of inversion. The microscopic interpretation is less constrained for ^{37}Na, but its calculated decay rate likewise depends on substantial accessible strength at favorable excitation energies. The broader implication is that large decay energies do not by themselves impose a universal millisecond half-life: identifying the fastest β emitters requires more than selecting the largest Q_β or the nucleus closest to the neutron drip line. The present results provide new benchmarks for theoretical descriptions of weakly bound nuclei and show that β-decay lifetimes remain sensitive to shell evolution at the limits of nuclear existence. While the absolute lower limit for a nuclear β-decay half-life remains an open question, addressing it requires understanding the interplay between the available decay energy and the underlying nuclear structure. Our measurements of ^{31}F and ^{37}Na extend these tests to exceptionally short half-lives, providing a basis for exploring how far structural effects persist and guiding the search for still faster β decays.

Methods

Beam production and experimental setup

The experiment was performed at FRIB utilizing the high-resolution focal plane of FDSi. Neutron-rich nuclei were produced by fragmentation of a ^{48}Ca primary beam at 225 MeV per nucleon and a beam power of approximately 10 kW on a rotating, 8-mm-thick carbon target. The reaction products were separated and transported through the preseparator and downstream separator of the Advanced Rare Isotope Separator (ARIS)[39]. Two separator settings, centered on ^{37}Na and ^{45}P, were used to deliver neutron-rich secondary cocktail beams to FDSi.

The diagnostic cross, located 2.5 m upstream of the implantation detector, housed a 2-mm-thick fast-timing scintillator coupled to a silicon photomultiplier (SiPM), followed by two silicon PIN detectors for energy-loss measurements. Both PIN detectors were 500 μm thick, with active areas of 4×4 cm^2 and 10×10 cm^2, respectively. The ion time of flight (ToF) was measured between a timing scintillator in the upstream ARIS DB3 diagnostic box and the SiPM-coupled scintillator. Combining this ToF with the energy loss, ΔE, measured in the second PIN detector provided event-by-event particle identification[40].

The identified ions were implanted into a segmented, cerium-doped yttrium orthosilicate (YSO) scintillator. An aluminum degrader positioned upstream of the YSO adjusted the ion range to optimize the implantation depth within the active detector thickness. Two plastic scintillators, positioned immediately upstream and downstream of the YSO, distinguished ions that stopped in the implantation detector from lighter ions that passed through it.

The implantation region was surrounded by 11 DEGAi high-purity germanium (HPGe) clover detectors and 11 $LaBr_3$(Ce) fast-timing detectors for γ-ray detection. On the south side of the YSO, 88 VANDLE neutron-detector modules were arranged in two layers at flight distances of approximately 90 and 96 cm.

In total, 197 ^{31}F ions and 99 ^{37}Na ions were implanted into the YSO. The time differences between implantations and their correlated β decays were used to construct the decay-time distributions presented in this work.

Implantation detector

The implantation detector consisted of a 12-mm-thick yttrium orthosilicate crystal (Y_2SiO_5, YSO), segmented into a 24×24 array of 2-mm-square pixels. The crystal was coupled to a Hamamatsu H12700 position-sensitive photomultiplier tube (PSPMT), with 64 anodes arranged in an 8×8 array and a common dynode. A 2-mm-thick quartz

light diffuser placed between the crystal and the PSPMT distributed the scintillation light from each pixel across several anodes, enabling position reconstruction with sub-anode granularity[41].

The anode signals were combined through a resistive Anger-logic readout to produce four position-sensitive outputs. The common dynode signal provided the total light-output and timing information. All signals were digitized using 16-bit Pixie-16 modules (XIA) at a sampling rate of 250 MS/s[42].

Defining the total anode signal as $S = S[0] + S[1] + S[2] + S[3]$, the uncorrected normalized coordinates are

$$x_0 = \frac{S[1] + S[2]}{S} - 0.5, \; y_0 = \frac{S[0] + S[1]}{S} - 0.5. \tag{2}$$

A systematic dependence of the dynode energy response on reconstructed position was observed. The dependence was characterized by fitting the dynode energy as a function of x_0 and y_0 independently, and the resulting fit parameters were used to correct the position coordinates. The corrected coordinates are

$$x_{\mathrm{pos}} = \frac{x_0}{1 - 0.45\left(\frac{A_{\mathrm{dyn}}}{10^6}\right)^{0.6}}, \; y_{\mathrm{pos}} = \frac{y_0}{1 - 0.20\left(\frac{A_{\mathrm{dyn}}}{10^6}\right)^{0.6}}, \tag{3}$$

where A_{dyn} is the baseline-subtracted integral of the PSPMT dynode waveform. The baseline was estimated from the first ten digitized samples of each waveform. The coefficients 0.45 and 0.20 and the exponent 0.6 were obtained empirically from fits to the dynode energy dependence along the two detector axes.

Implant–decay correlations

Implantation events were identified by a low-gain YSO dynode signal in coincidence with a hit in the PIN detector. Decay events corresponded to the detection of the

β-electron and were identified by requiring a hit from the low- or high-gain dynode signal with an anticoincidence condition on the cross scintillator. Event positions were reconstructed from the anode signals, and event times were obtained from the dynode signals.

Position and time correlations between implantation and decay events were used to generate decay curves for the ions presented here. For each decay electron, all preceding implants with an implant–decay time difference $0 < \Delta t < 30$ ms and a spatial separation below 3.5 mm were stored in an implant list. Each candidate within the particle-identification gate for the isotope of interest contributed one entry at its implant–decay time difference to the corresponding decay-time histogram. Thus, a decay could contribute multiple entries when more than one implantation satisfied these criteria.

Decay-curve fits

Decay curves were fitted in the 0–30 ms interval using 0.50-ms bins and bin-integrated equations for parent decay and the growth and decay of the $\beta 0n$, $\beta 1n$, $\beta 2n$ and $\beta 3n$ daughters. The chains also include the granddaughter populated by the $\beta 0n$ daughter for ^{31}F, and the granddaughters populated by the $\beta 0n$ and $\beta 2n$ daughters for ^{37}Na. Because experimental β-delayed neutron-emission probabilities were unavailable, the frequentist fits fixed the $(\beta 0n, \beta 1n, \beta 2n, \beta 3n)$ branching fractions to $(0.00, 0.63, 0.17, 0.20)$ for ^{31}F and $(0.00, 0.51, 0.24, 0.25)$ for ^{37}Na, based on Ref.[31]; the Bayesian fit instead inferred normalized branching fractions under the priors specified below. The random-correlation background was estimated independently by pairing each implantation with β-like events recorded before it (negative correlation times), for which a causal implantation–decay correlation is impossible. The model is truncated at the $\beta 3n$ branch and therefore assumes that branches with $x \geq 4$ are negligible.

Bateman equations and decay chains

The time evolution of nuclei in each decay chain was modeled using the Bateman equations. A single parent can populate independent $\beta 0n$, $\beta 1n$, $\beta 2n$ and $\beta 3n$ daughter branches, each with a distinct decay constant and branching fraction. Selected daughters subsequently populate a granddaughter with unit branching in the implemented chain: the $\beta 0n$ daughter for ^{31}F, and the $\beta 0n$ and $\beta 2n$ daughters for ^{37}Na.

Parent nucleus

The population of the parent nucleus as a function of time t is

$$N_{\mathrm{p}}(t) = N_0\, e^{-\lambda_{\mathrm{p}} t},$$

where N_0 is the initial number of parent nuclei and $\lambda_{\mathrm{p}} = \ln 2 / T_{1/2}^{\mathrm{parent}}$ is the parent decay constant.

Single-step daughter nuclei

Each daughter is assumed to be populated directly by the decay of the parent. The number of daughter nuclei in branch i at time t is

$$N_{\mathrm{d},i}(t) = N_0\, b_i \left(\frac{\lambda_{\mathrm{p}}}{\lambda_{\mathrm{d},i} - \lambda_{\mathrm{p}}} \right) \left(e^{-\lambda_{\mathrm{p}} t} - e^{-\lambda_{\mathrm{d},i} t} \right), \qquad i = 0, 1, 2, 3,$$

where b_i is the branching fraction to branch i and $\lambda_{\mathrm{d},i}$ is the decay constant of the corresponding daughter nucleus.

Granddaughter nuclei

The fitted normalization A_0 is the detected parent count rate at $t = 0$, in counts ms^{-1}; it absorbs the initial parent population and the common β-detection efficiency

assumed for the parent, daughter and granddaughter components. For an included granddaughter fed by daughter branch i, the detected rate is

$$R_{g,i}(t) = A_0 b_i c_i \lambda_{\mathrm{d},i} \lambda_{g,i} \left[\frac{e^{-\lambda_\mathrm{p} t}}{(\lambda_{\mathrm{d},i} - \lambda_\mathrm{p})(\lambda_{g,i} - \lambda_\mathrm{p})} + \frac{e^{-\lambda_{\mathrm{d},i} t}}{(\lambda_\mathrm{p} - \lambda_{\mathrm{d},i})(\lambda_{g,i} - \lambda_{\mathrm{d},i})} + \frac{e^{-\lambda_{g,i} t}}{(\lambda_\mathrm{p} - \lambda_{g,i})(\lambda_{\mathrm{d},i} - \lambda_{g,i})} \right].$$

Here, $\lambda_{g,i}$ is the granddaughter decay constant and c_i is the daughter-to-granddaughter branching fraction. We fix $c_i = 1$ as a simplifying approximation, assigning unit feeding to the specified granddaughter and omitting competing daughter-decay branches from the model.

Decay rates

The decay rate (or activity) of each component is

$$R_i(t) = \lambda_i N_i(t),$$

where λ_i is the decay constant and $N_i(t)$ is the population of the ith component at time t.

The total detected decay rate fitted to the experimental time spectrum is

$$R_\mathrm{total}(t) = R_\mathrm{parent}(t) + \sum_{i=0}^{3} R_{\beta in}(t) + \sum_{i \in \mathcal{G}} R_{g,i}(t) + R_\mathrm{background}(t),$$

where $\mathcal{G} = \{0\}$ for ^{31}F and $\mathcal{G} = \{0, 2\}$ for ^{37}Na.

Fit parameters and background estimation

In the frequentist fits, the $\beta 0n$, $\beta 1n$, $\beta 2n$ and $\beta 3n$ branching ratios were fixed to values calculated in Ref.[31]. The active daughter and granddaughter decay constants

were fixed to literature values. The parent activity was free, and the background was fixed by the average background rate from the reverse-time correlations. These fits gave 1.45 ± 0.22 ms for ^{31}F and 1.58 ± 0.25 ms for ^{37}Na.

Bayesian analysis

Model specification

For the observed count N_k in the bin with edges t_k and t_{k+1}, the Bayesian model was

$$N_k \sim \text{Poisson}(\mu_k), \tag{4}$$

$$\mu_k = \int_{t_k}^{t_{k+1}} \left[R_\text{p}(t) + \sum_{i=0}^{3} R_{\text{d},i}(t) + \sum_{i \in \mathcal{G}} R_{g,i}(t) + B \right] dt, \tag{5}$$

$$T_{1/2}^{\text{par}} \sim \mathcal{TN}_{(0,\infty)}(5.0, 5.0^2), \tag{6}$$

$$T_{\text{d},i} \sim \mathcal{TN}_{(0,\infty)}(\overline{T}_{\text{d},i}, \sigma^2_{T_{\text{d},i}}), \qquad i \in \mathcal{D}, \tag{7}$$

$$T_{g,i} \sim \mathcal{TN}_{(0,\infty)}(\overline{T}_{g,i}, \sigma^2_{T_{g,i}}), \qquad i \in \mathcal{G}, \tag{8}$$

$$u_j \sim \text{Uniform}(0,1), \qquad j = 0,1,2,3, \tag{9}$$

$$b_j = \frac{u_j}{\sum_{\ell=0}^{3} u_\ell}, \tag{10}$$

$$A_0 \sim \text{LogNormal}\left(\ln \overline{A}_0, 0.75^2\right), \tag{11}$$

$$B \sim \text{Uniform}\left(0.50\,\overline{B}, 1.50\,\overline{B}\right). \tag{12}$$

Here, $\mathcal{TN}_{(a,b)}(\mu, \sigma^2)$ denotes a normal distribution with location μ and standard deviation σ, truncated to (a, b); $\mathcal{D} = \{0,1,2,3\}$ indexes the daughter branches. For both nuclei, the parent-half-life prior had location and standard deviation 5.0 ms and was truncated at zero. For the daughters ordered as $\beta 0n$, $\beta 1n$, $\beta 2n$ and $\beta 3n$, the prior location and standard-deviation pairs were $(3.4, 0.8)$, $(7.3, 0.3)$, $(14.0, 0.5)$ and $(18.7, 0.2)$ ms for ^{31}F, and $(6.4, 1.6)$, $(7.2, 1.2)$, $(11.3, 0.6)$ and $(44.9, 0.4)$ ms for ^{37}Na. The ^{31}F chain used $T_{g,0} = 17.0 \pm 0.2$ ms. The ^{37}Na chain used $T_{g,0} = 11.4 \pm 0.3$ ms and

$T_{g,2} = 38.4 \pm 0.3$ ms. The numerical values listed here specify the literature-informed priors used in the fits; evaluated decay information for these nuclides is available from NuDat3[13]. Each raw branch weight u_j was independently uniform on $(0, 1)$, and normalizing the four weights enforced $\sum_j b_j = 1$. The log-normal A_0 priors used early-time estimates $\overline{A}_0 = 36.01$ and 24.02 counts ms^{-1} for ^{31}F and ^{37}Na, respectively, as their median values. The reverse-time background estimates were $\overline{B} = 3.99$ and 1.98 counts ms^{-1}, respectively, with uniform priors spanning $\overline{B} \times (1 \pm 0.50)$.

Posterior sampling and summaries

Posterior inference used the No-U-Turn Sampler (NUTS) implemented in `PyMC` version 5.25.1[43]. For each nucleus, eight chains were run with 10,000 tuning iterations followed by 30,000 retained iterations per chain, giving 240,000 retained posterior draws. The target acceptance probability was 0.95 and the random seed was 42; neither fit contained a divergence or reached the maximum tree depth.

For the present Bayesian analysis, quoted half-lives are posterior medians with central 68% credible intervals, defined by the 16th and 84th percentiles of the marginal posterior distributions. Central 95% credible intervals are bounded by the 2.5th and 97.5th percentiles. For fitted decay curves, these intervals are evaluated pointwise from the posterior distribution of the expected counts. The one-dimensional intervals in Extended Data Figs. 1–3 use the same definition. Posterior means and standard deviations are reported separately in Extended Data Table 2. The daughter and granddaughter half-life posteriors remain centered on their literature-based priors, whereas the neutron branching probabilities are broad owing to the limited statistics and similar daughter half-lives. Parameter correlations were quantified from the posterior samples using the Pearson correlation coefficient, ρ[44]. For ^{31}F, the parent half-life is anticorrelated with the initial activity ($\rho = -0.72$) and background ($\rho = -0.35$), and positively correlated with the total neutron-emission probability, $P_{\Sigma n}$ ($\rho = 0.34$).

For ^{37}Na, the corresponding correlations are $\rho = -0.68$, -0.26 and 0.20, respectively. All other correlations involving the parent half-life, including those with the daughter and granddaughter half-lives and the individual neutron-emission probabilities, have $|\rho| < 0.1$. The strong anticorrelation with the initial activity reflects the trade-off between the normalization and decay-time scale of the early-time spectrum when the number of implanted ions is limited. Posterior distributions and parameter correlations are shown in Extended Data Figs. 1 and 2.

Shortest measured β-decay half-lives

Extended Data Table 1 ranks experimental nuclear β^--decay half-lives by central value, using NUBASE2020[32] as the starting evaluation and checking subsequent measurements through 20 September 2026. Estimates inferred from systematics and lifetime limits are excluded. Overlapping entries were replaced by the values from the FRIB measurements of Crawford et al.[24]; in particular, the older ^{35}Na value of 1.5 ± 0.5 ms is replaced by $2.4 \pm 0.3 \pm 0.2$ ms. The newly measured ^{38}Mg and ^{41}Al half-lives[24] and the ^{61}Sc and ^{63}Ti measurements of Ong et al.[45] also enter the ten shortest values. The ^{31}Ne value is retained but flagged as tentative in the current evaluation[46].

The comparison concerns the parent β^--decay rate, including all β-delayed particle-emission branches. A short total lifetime dominated by a competing decay mode is not counted as a short β^- half-life: for a mixed-mode state, the partial half-life is $T_{1/2}^{\beta^-} = T_{1/2}^{\mathrm{total}}/b_{\beta^-}$, where b_{β^-} is the total β^- branching fraction. Ground and isomeric states were checked separately.

Detailed shell-model calculations

Hamiltonians and model spaces

Calculations in the $N \simeq 20$ region were carried out with SDPF-M, whereas those toward $N \simeq 28$ used SDPFSDG-MU. For each interaction, the parent and daughter

wave functions were obtained by diagonalizing the same Hamiltonian in the specified proton and neutron valence spaces. The SDPF-M calculation for ^{31}F included configurations up to $2\hbar\omega$, retaining the cross-shell configurations required to describe the island-of-inversion region. In the SDPFSDG-MU calculations, the parent and daughter spaces were selected according to the $n\hbar\omega$ truncation appropriate to each nucleus. In particular, the framework used here is reliable for the $0\hbar\omega$ parent configurations in the $N \geq 24$ region and the associated daughter configurations reached by the GT operator. If a $1\hbar\omega$ configuration becomes dominant in the parent, important daughter configurations can occur in the $2\hbar\omega$ space and are absent from the present truncation; results in that regime were therefore not used for the principal interpretation.

Parent and daughter states

For a parent state with spin J_i and parity π_i, daughter states with $J_f = J_i$ or $J_i \pm 1$ and $\pi_f = \pi_i$ were included, excluding a $0 \to 0$ GT transition. Opposite-parity daughter states connected by the rank-0, rank-1 and rank-2 FF operators were included in the FF part of the rate. When the parent ground-state spin and parity were uncertain, the calculation was repeated for each candidate assignment and the predictions were displayed separately. Daughter eigenstates were calculated to cover the full $Q(\beta^-)$ window, and only states satisfying $E_{x,f} < Q(\beta^-)$ contribute to the total rate.

Gamow–Teller strengths

Following Ref.[26], the reduced transition strength was defined as

$$B(\mathrm{GT}; i \to f) \equiv \frac{1}{2J_i + 1} \left| \langle f \, \| q_{\mathrm{GT}} \boldsymbol{\sigma} t_- \| \, i \rangle \right|^2 . \tag{13}$$

Here $\boldsymbol{\sigma} t_-$ denotes the many-body GT operator, with the convention $t_- |n\rangle = |p\rangle$, and the quenching factor is included in the operator itself. Thus, relative to an unquenched calculation, the strength is reduced by q_{GT}^2.

Phase-space factors and total half-lives

The dimensionless Fermi integral for an allowed transition was evaluated as

$$f_0 = \int_1^{W_0} F(Z,W)\sqrt{W^2-1}\,W(W_0-W)^2\,dW, \tag{14}$$

where W is the total energy of the emitted electron in units of $m_e c^2$ and $F(Z,W)$ is the Fermi function describing Coulomb distortion of the electron wave function. The maximum electron energy was

$$W_0 = Q(\beta^-) + 1 - E_x, \tag{15}$$

where both $Q(\beta^-)$ and E_x are expressed in units of $m_e c^2$. For a transition $i \to f$, the partial half-life was calculated as

$$f_0 t_{i\to f}^{\mathrm{GT}} = \frac{K}{(g_A/g_V)^2 B(\mathrm{GT}; i\to f)}, \qquad K = 6144 \pm 2\ \mathrm{s}, \quad \frac{g_A}{g_V} = -1.2701(25). \tag{16}$$

Because f_0 is approximately proportional to the fifth power of the endpoint energy, moderate GT strengths at low daughter excitation energy can make a dominant contribution to the total rate.

First-forbidden contributions

The FF contribution included in the total half-life was evaluated following Ref.[26]. For each FF transition,

$$f^{\mathrm{FF}} t_{i\to f}^{\mathrm{FF}} = K, \qquad f^{\mathrm{FF}} = \sum_{R=0,1,2} f_{\mathrm{FF}}^{(R)}, \tag{17}$$

with

$$f_{\mathrm{FF}}^{(R)} = \int_1^{W_0} C^{(R)}(W) F(Z,W) \sqrt{W^2-1}\, W (W_0 - W)^2 \, dW, \tag{18}$$

where $C^{(R)}(W)$ is the rank-R shape factor. The sum in Eq. (1) contains the partial half-lives of both GT and FF transitions. The effective-operator scaling factors were 1.0, 1.7, 1.0, 1.0 and 0.55 for M_0^S, M_0^T, x, u and z, respectively, as in Ref.[26].

Decay and excitation energies

Two endpoint-energy prescriptions were compared for the shell-model calculations. The adopted-value prescription uses mass-evaluation $Q(\beta^-)$ values, including extrapolated estimates where masses are unmeasured, together with shell-model daughter excitation energies and transition matrix elements. This prescription is used for the shell-model predictions in Fig. 3 and the filled-circle curves in Fig. 4. The theoretical prescription uses the shell-model value evaluated as

$$Q(\beta^-) = E_{\mathrm{g.s.}}^{\mathrm{par.}} - E_{\mathrm{g.s.}}^{\mathrm{dau.}} + \delta m, \qquad \delta m = (m_n - m_p - m_e)c^2 = 0.78 \text{ MeV}, \tag{19}$$

where bound-state energies follow the convention $E < 0$. For a shell-model Hamiltonian without the Coulomb interaction, the energy entering Eq. (19) was obtained from

$$E = E_{\mathrm{SM}} + E_C(Z,N), \tag{20}$$

with

$$E_C(Z,N) = 0.700 \, \frac{Z(Z-1) - 0.76[Z(Z-1)]^{2/3}}{R_C} \text{ MeV}, \tag{21}$$

$$R_C = e^{1.5/A} A^{1/3} \left[0.946 - 0.573 \left(\frac{2T}{A} \right)^2 \right], \qquad T = \frac{|Z-N|}{2}. \tag{22}$$

In both endpoint-energy prescriptions, the excitation energies E_x in Eq. (15) were taken from the shell-model calculation. No transition with $W_0 \leq 1$ was retained. The resulting pair of predictions isolates the sensitivity of the calculated half-life to the nuclear masses.

The experimental and theoretical Q_β calculations use identical shell-model wave functions and transition matrix elements. Their difference therefore probes endpoint-energy sensitivity, whereas comparisons among interactions, truncations and candidate parent spin-parity assignments probe model dependence. These variations are displayed as separate predictions and are not treated as a statistical confidence interval.

Systematics of the calculated half-lives

Extended Data Fig. 4 compares calculations for the neutron-rich F and Na isotopes. The shell-model predictions in the left and right panels use adopted mass-evaluation and shell-model Q_β values, respectively. SDPF-M and SDPFSDG-MU calculations are denoted by triangles and pentagons, and multiple open symbols for an isotope represent alternative candidate ground-state spin-parity assignments. The filled symbols show measured values, including the first half-life measurements of ^{31}F and ^{37}Na and the ^{35}Na validation measurement; the remaining experimental values are from NUBASE2020[32] and Ref.[24].

SDPFSDG-MU results are omitted for cases such as Na isotopes with $N \leq 23$ when the calculated parent ground state is dominated by $1\hbar\omega$ configurations. The corresponding GT-fed $2\hbar\omega$ daughter states lie outside the adopted model space, so their omission would make the rate incomplete. SDPF-M is therefore used in this region, whereas SDPFSDG-MU is adopted for the $N \geq 24$ systems relevant to ^{37}Na.

Cumulative rates and structural interpretation

To clarify how transitions to daughter states at different excitation energies build up the total decay rate, we calculated the cumulative decay rate as a function of daughter excitation energy. Both GT and FF transitions were included, so that the cumulative rate directly shows which excitation-energy regions contribute to the calculated half-life. For an excitation-energy cutoff E, the cumulative decay rate was defined as

$$\lambda_{\mathrm{cum}}(E) = \sum_{\substack{f\in\mathrm{GT}\\ E_{x,f}\le E}} \frac{1}{t^{\mathrm{GT}}_{i\to f}} + \sum_{\substack{f\in\mathrm{FF}\\ E_{x,f}\le E}} \frac{1}{t^{\mathrm{FF}}_{i\to f}} \tag{23}$$

The ^{19}B reference calculation used YSOX[37], the ^{31}F calculation used SDPF-M in the $2\hbar\omega$ space, and the ^{37}Na calculation used SDPFSDG-MU within $1\hbar\omega$. The cumulative decay rates for all three nuclei in Fig. 4 were evaluated consistently using Eq. (23).

The measured ^{19}B half-life is 2.92(13) ms[38], more than twice the measured ^{31}F value even though its $Q_\beta = 27.4$ MeV is approximately 1.8 MeV larger[27]. In the calculation, a few strong GT transitions to ^{19}C states near 2–3 MeV dominate the ^{19}B rate. No single transition dominates ^{31}F; instead, the calculated decay rate accumulates through transitions to low-lying ^{31}Ne states below approximately 5 MeV, with further contributions between 5 and 10 MeV. For the GT component, lower excitation energies correspond to larger effective endpoints, $Q_{\mathrm{eff}} = Q_\beta - E_x$, and hence to larger allowed-decay phase-space factors. The cumulative rate calculated for ^{37}Na similarly builds up across low and intermediate excitation energies, with both GT and FF contributions included. This comparison motivates the structure-enabled phase-space interpretation in the main text while avoiding a unique inference of parent spin-parity or wave-function composition from a half-life alone.

Data availability

The decay data and figures are available from the corresponding author upon request.

Code availability

Shell-model calculations were performed using the publicly available KSHELL code[47,48] and NuclearToolkit.jl[49]. The Bayesian half-life analysis software is archived as version v0.1.0 on Zenodo[50]. The development repository is available on GitHub. The run inputs and posterior outputs supporting this study are available from the corresponding author upon request.

References

1. Erler, J. *et al.* The limits of the nuclear landscape. *Nature* **486**, 509–512 (2012). URL https://doi.org/10.1038/nature11188.

2. Tsunoda, N. *et al.* The impact of nuclear shape on the emergence of the neutron dripline. *Nature* **587**, 66–71 (2020). URL https://doi.org/10.1038/s41586-020-2848-x.

3. Otsuka, T., Gade, A., Sorlin, O., Suzuki, T. & Utsuno, Y. Evolution of shell structure in exotic nuclei. *Rev. Mod. Phys.* **92**, 015002 (2020). URL https://doi.org/10.1103/RevModPhys.92.015002.

4. Neufcourt, L. *et al.* Quantified limits of the nuclear landscape. *Phys. Rev. C* **101**, 044307 (2020). URL https://doi.org/10.1103/PhysRevC.101.044307.

5. Mayer, M. G. On closed shells in nuclei. II. *Phys. Rev.* **75**, 1969–1970 (1949). URL https://doi.org/10.1103/PhysRev.75.1969.

6. Sorlin, O. & Porquet, M.-G. Nuclear magic numbers: new features far from stability. *Prog. Part. Nucl. Phys.* **61**, 602–673 (2008). URL https://doi.org/10.1016/j.ppnp.2008.05.001.

7. Ozawa, A., Kobayashi, T., Suzuki, T., Yoshida, K. & Tanihata, I. New magic number, $N = 16$, near the neutron drip line. *Phys. Rev. Lett.* **84**, 5493–5495 (2000). URL https://doi.org/10.1103/PhysRevLett.84.5493.

8. Bertsch, G. F. & Esbensen, H. Pair correlations near the neutron drip line. *Ann. Phys.* **209**, 327–363 (1991). URL https://doi.org/10.1016/0003-4916(91)90033-5.

9. Engel, J., Bender, M., Dobaczewski, J., Nazarewicz, W. & Surman, R. β decay rates of r-process waiting-point nuclei in a self-consistent approach. *Phys. Rev. C* **60**, 014302 (1999).

10. Fossez, K. & Rotureau, J. Density matrix renormalization group description of the island of inversion isotopes $^{28-33}$F. *Phys. Rev. C* **106**, 034312 (2022). URL https://doi.org/10.1103/PhysRevC.106.034312.

11. Zhang, K. Y. *et al.* Collapse of the $N = 28$ shell closure in the newly discovered ^{39}Na nucleus and the development of deformed halos towards the neutron dripline. *Phys. Rev. C* **107**, L041303 (2023). URL https://doi.org/10.1103/PhysRevC.107.L041303.

12. Tanihata, I., Savajols, H. & Kanungo, R. Recent experimental progress in nuclear halo structure studies. *Prog. Part. Nucl. Phys.* **68**, 215–313 (2013). URL https://doi.org/10.1016/j.ppnp.2012.07.001.

13. National Nuclear Data Center. NuDat 3: Nuclear Structure and Decay Data. https://www.nndc.bnl.gov/nudat3/ (2026). Brookhaven National Laboratory.

14. Stroberg, S. R., Holt, J. D., Schwenk, A. & Simonis, J. Ab initio limits of atomic nuclei. *Phys. Rev. Lett.* **126**, 022501 (2021). URL https://doi.org/10.1103/PhysRevLett.126.022501.

15. Warburton, E. K., Becker, J. A. & Brown, B. A. Mass systematics for $A = 29$–44 nuclei: the deformed $A \sim 32$ region. *Phys. Rev. C* **41**, 1147–1166 (1990). URL https://doi.org/10.1103/PhysRevC.41.1147.

16. Ahn, D. S. *et al.* Location of the neutron dripline at fluorine and neon. *Phys. Rev. Lett.* **123**, 212501 (2019). URL https://doi.org/10.1103/PhysRevLett.123.212501.

17. Nowacki, F. & Caurier, E. Shell model and nuclear structure far from stability. *Acta Phys. Pol. B* **30**, 749–753 (1999). URL https://www.actaphys.uj.edu.pl/R/30/3/749/pdf.

18. Utsuno, Y., Otsuka, T., Mizusaki, T. & Honma, M. Extreme location of F drip line and disappearance of the magic structure. *Phys. Rev. C* **64**, 011301 (2001). URL https://doi.org/10.1103/PhysRevC.64.011301.

19. Sakurai, H. *et al.* Evidence for particle stability of ^{31}F and particle instability of ^{25}N and ^{28}O. *Phys. Lett. B* **448**, 180–184 (1999). URL https://doi.org/10.1016/S0370-2693(99)00015-5.

20. Caurier, E., Nowacki, F. & Poves, A. Merging of the islands of inversion at $N = 20$ and $N = 28$. *Phys. Rev. C* **90**, 014302 (2014). URL https://doi.org/10.1103/PhysRevC.90.014302.

21. Notani, M. *et al.* New neutron-rich isotopes, ^{34}Ne, ^{37}Na and ^{43}Si, produced by fragmentation of a 64 A MeV ^{48}Ca beam. *Phys. Lett. B* **542**, 49–54 (2002). URL https://doi.org/10.1016/S0370-2693(02)02337-7.

22. Lukyanov, S. M. *et al.* Experimental evidence for the particle stability of ^{34}Ne and ^{37}Na. *J. Phys. G* **28**, L41–L45 (2002). URL https://doi.org/10.1088/0954-3899/28/9/101.

23. Ahn, D. S. *et al.* Discovery of ^{39}Na. *Phys. Rev. Lett.* **129**, 212502 (2022). URL https://doi.org/10.1103/PhysRevLett.129.212502.

24. Crawford, H. L. *et al.* Crossing $N = 28$ toward the neutron drip line: first measurement of half-lives at FRIB. *Phys. Rev. Lett.* **129**, 212501 (2022). URL https://doi.org/10.1103/PhysRevLett.129.212501.

25. Takahashi, K. & Yamada, M. Gross theory of nuclear β-decay. *Prog. Theor. Phys.* **41**, 1470–1503 (1969). URL https://doi.org/10.1143/PTP.41.1470.

26. Yoshida, S., Utsuno, Y., Shimizu, N. & Otsuka, T. Systematic shell-model study of β-decay properties and Gamow–Teller strength distributions in $A \approx 40$ neutron-rich nuclei. *Phys. Rev. C* **97**, 054321 (2018). URL https://doi.org/10.1103/PhysRevC.97.054321.

27. Wang, M., Huang, W. J., Kondev, F. G., Audi, G. & Naimi, S. The AME 2020 atomic mass evaluation (II). Tables, graphs and references. *Chin. Phys. C* **45**, 030003 (2021). URL https://doi.org/10.1088/1674-1137/abddaf.

28. Algora, A., Tain, J. L., Rubio, B., Fallot, M. & Gelletly, W. β-decay studies for applied and basic nuclear physics. *Eur. Phys. J. A* **57**, 85 (2021).

29. FRIB Decay Station Initiator proposal (2020). URL https://fds.ornl.gov/wp-content/uploads/2020/09/FDSi-Proposal-May2020.pdf.

30. Allmond, J. M. & Grzywacz, R. The FRIB Decay Station: new horizons with rare isotopes. *Nucl. Phys. News* **35**, 24–27 (2025). URL https://doi.org/10.1080/10619127.2025.2454222.

31. Möller, P., Mumpower, M. R., Kawano, T. & Myers, W. D. Nuclear properties for astrophysical and radioactive-ion-beam applications (II). *At. Data Nucl. Data Tables* **125**, 1–192 (2019). URL https://doi.org/10.1016/j.adt.2018.03.003.

32. Kondev, F. G., Wang, M., Huang, W. J., Naimi, S. & Audi, G. The NUBASE2020 evaluation of nuclear physics properties. *Chin. Phys. C* **45**, 030001 (2021). URL https://doi.org/10.1088/1674-1137/abddae.

33. Japan Atomic Energy Agency, Nuclear Data Center. Estimation of beta-decay properties. URL https://wwwndc.jaea.go.jp/nucldata/beta-decay-properties.pdf. Accessed 20 September 2026.

34. Utsuno, Y., Otsuka, T., Mizusaki, T. & Honma, M. Varying shell gap and deformation in $N \sim 20$ unstable nuclei studied by the Monte Carlo shell model. *Phys. Rev. C* **60**, 054315 (1999). URL https://doi.org/10.1103/PhysRevC.60.054315.

35. Yoshida, S., Utsuno, Y., Shimizu, N. & Otsuka, T. Erratum: Systematic shell-model study of β-decay properties and Gamow–Teller strength distributions in $A \approx 40$ neutron-rich nuclei [Phys. Rev. C **97**, 054321 (2018)]. *Phys. Rev. C* **109**, 029904 (2024). URL https://doi.org/10.1103/PhysRevC.109.029904.

36. Utsuno, Y. *et al.* Shape transitions in exotic Si and S isotopes and tensor-force-driven Jahn–Teller effect. *Phys. Rev. C* **86**, 051301 (2012). URL https://doi.org/10.1103/PhysRevC.86.051301.

37. Yuan, C., Suzuki, T., Otsuka, T., Xu, F. & Tsunoda, N. Shell-model study of boron, carbon, nitrogen, and oxygen isotopes with a monopole-based universal interaction. *Phys. Rev. C* **85**, 064324 (2012). URL https://doi.org/10.1103/PhysRevC.85.064324.

38. Yoneda, K. *et al.* β-decay half-lives and β-delayed neutron multiplicities of the neutron drip-line nuclei ^{19}B, ^{22}C and ^{23}N. *Phys. Rev. C* **67**, 014316 (2003). URL https://doi.org/10.1103/PhysRevC.67.014316.

39. Portillo, M. *et al.* Commissioning of the Advanced Rare Isotope Separator ARIS at FRIB. *Nucl. Instrum. Methods Phys. Res. B* **540**, 151–157 (2023). URL https://doi.org/10.1016/j.nimb.2023.04.025.

40. Tarasov, O. B. *et al.* Production of very neutron-rich nuclei with a ^{76}Ge beam. *Phys. Rev. C* **80**, 034609 (2009). URL https://doi.org/10.1103/PhysRevC.80.034609.

41. Yokoyama, R. *et al.* Segmented YSO scintillation detectors as a new β-implant detection tool for decay spectroscopy in fragmentation facilities. *Nucl. Instrum. Methods Phys. Res. A* **937**, 93–97 (2019). URL https://doi.org/10.1016/j.nima.2019.05.026.

42. XIA LLC. Pixie-16 user manual, version 3.06 (2019). URL https://download.xia.com/products/pixie16/documents/manuals/XIA-Pixie16-Users-Manual-3.06-2019-09-13.pdf.

43. Abril-Pla, O. *et al.* PyMC: a modern and comprehensive probabilistic programming framework in Python. *PeerJ Comput. Sci.* **9**, e1516 (2023). URL https://doi.org/10.7717/peerj-cs.1516.

44. Pearson, K. VII. Note on regression and inheritance in the case of two parents. *Proceedings of the Royal Society of London* **58**, 240–242 (1895).

45. Ong, W.-J. *et al.* Beta-decay half-lives beyond ^{54}Ca: a systematic survey of decay properties approaching the neutron dripline. *Phys. Rev. Lett.* **136**, 092502 (2026). URL https://doi.org/10.1103/5yrq-s3g5.

46. Chen, J. & Singh, B. Adopted levels of ^{31}Ne. Evaluated Nuclear Structure Data File, National Nuclear Data Center (2022). URL https://www.nndc.bnl.gov/ensnds/31/Ne/adopted.pdf. Evaluation dated June 2022; Nuclear Data Sheets 184, 29 (2022). Accessed 20 September 2026.

47. Shimizu, N. Nuclear shell-model code for massive parallel computation, "KSHELL" (2013). Preprint at https://arxiv.org/abs/1310.5431.

48. Shimizu, N., Mizusaki, T., Utsuno, Y. & Tsunoda, Y. Thick-restart block Lanczos method for large-scale shell-model calculations. *Comput. Phys. Commun.* **244**, 372–384 (2019). URL https://doi.org/10.1016/j.cpc.2019.06.011.

49. Yoshida, S. NuclearToolkit.jl: a Julia package for nuclear structure calculations. *J. Open Source Softw.* **7**, 4694 (2022). URL https://doi.org/10.21105/joss.04694.

50. tawfikgaballah. tawfikgaballah/Bayesian-Inference-for–Decay-Half-Lives: Initial standalone release of the browser-based decay-chain Bayesian analysis GUI. Zenodo (2026). URL https://doi.org/10.5281/zenodo.20710417. Version v0.1.0.

Funding

This work was supported by the National Science Foundation under Grants No. PHY-2412343 (Mississippi State), No. PHY-1848177 (CAREER; Mississippi State), No. PHY-2012522 (FSU), and Major Research Instrumentation Program Award No. 1919735 (UTK). This work was also supported by the U.S. Department of Energy, Office of Science, Office of Nuclear Physics, under Contract No. DE-SC0014448 (Mississippi State), Award No. DE-SC0023633, and Contracts No. DE-SC0020451 (Michigan State), No. DE-AC02-06CH11357 (ANL), No. DE-AC02-98CH10946 (BNL), No. DE-AC02-05CH11231 (LBNL), No. DE-AC52-07NA27344 (LLNL), No. DE-AC05-00OR22725 (ORNL), and No. DE-FG02-96ER40983 (UTK).

This work was supported in part by JSPS Grant-in-Aid for Scientific Research (Grant Nos. JP22K14030, JP25H01511) and JST PRESTO (Grant No. JPMJPR25F8).

This work was further supported by the U.S. Department of Energy, National Nuclear Security Administration, under Awards No. DE-NA0004249 and No. DE-NA0003180, including through the Nuclear Science and Security Consortium, and by the Stewardship Science Academic Alliances (SSAA) Program under Awards No. DE-NA0003906 (Michigan State) and No. DE-NA0003899 (UTK).

This work used resources of the Facility for Rare Isotope Beams (FRIB), a U.S. Department of Energy Office of Science User Facility.

Author contributions

T. Gaballah: *Data analysis, software, manuscript writing, and experiment execution.*

B. P. Crider: *Study design, funding acquisition, supervision, manuscript writing, and experiment execution.*

H. L. Crawford: *Study design, instrumentation, data analysis, manuscript revision, and experiment execution.*

S. N. Liddick: *Study design, supervision, instrumentation, experiment execution, and manuscript revision.*

S. Yoshida: *Theoretical calculations and manuscript writing.*

J. M. Allmond: *Study design, instrumentation, experiment execution, and manuscript revision.*

R. Grzywacz: *Study design, instrumentation, experiment execution, and manuscript revision.*

V. Tripathi: *Study design, instrumentation, and experiment execution.*

Y. Utsuno: *Theoretical calculations.*

S. O. Ajayi: *Experiment execution.*

A. Andalib: *Experiment execution.*

C. J. Appleton: *Experiment execution.*

E. Argo: *Experiment execution.*

H. Arora: *Experiment execution.*

P. C. Bender: *Experiment execution.*

C. B. Benetti: *Experiment execution.*

J. M. Berkman: *Experiment execution.*

S. Bhattacharya: *Experiment execution.*

N. Braukman: *Experiment execution.*

C. M. Campbell: *Experiment execution.*

M. P. Carpenter: *Experiment execution.*

J. Chan: *Experiment execution.*

A. Chester: *Software and experiment execution.*

J. M. Christie: *Experiment execution.*

B. R. Clark: *Experiment execution.*

R. M. Clark: *Experiment execution.*

I. Cox: *Experiment execution and manuscript revision.*

A. Doetsch: *Experiment execution and data analysis.*

J. Dopfer: *Experiment execution.*

J. G. Duarte: *Experiment execution.*

P. Fallon: *Experiment execution and manuscript revision.*

A. Frotscher: *Experiment execution.*

T. J. Gray: *Experiment execution.*

J. T. Harke: *Experiment execution.*

J. Heideman: *Experiment execution.*

H. Heugen: *Experiment execution.*

R. Jain: *Experiment execution.*

T. T. King: *Experiment execution and instrumentation.*

N. Kitamura: *Experiment execution.*

K. Kolos: *Experiment execution.*

F. G. Kondev: *Experiment execution.*

A. Laminack: *Experiment execution.*

B. Longfellow: *Experiment execution and manuscript revision.*

R. S. Lubna: *Experiment execution and instrumentation.*

S. Luitel: *Experiment execution.*

M. Madurga: *Experiment execution and manuscript revision.*

R. Mahajan: *Experiment execution.*

M. J. Mogannam: *Experiment execution.*

S. K. Neupane: *Experiment execution.*

A. Nowicki: *Experiment execution.*

T. H. Ogunbeku: *Experiment execution.*

W. J. Ong: *Experiment execution.*

C. Porzio: *Experiment execution.*

C. J. Prokop: *Experiment execution.*

B. C. Rasco: *Experiment execution.*

E. K. Ronning: *Experiment execution and manuscript revision.*

E. Rubino: *Experiment execution.*

T. J. Ruland: *Experiment execution.*

K. P. Rykaczewski: *Experiment execution.*

L. Schaedig: *Experiment execution.*

D. P. Scriven: *Experiment execution.*

D. Seweryniak: *Experiment execution.*

K. Siegl: *Experiment execution.*

M. Singh: *Experiment execution.*

A. Spyrou: *Experiment execution and manuscript revision.*

S. L. Tabor: *Experiment execution and manuscript revision.*

T. L. Tang: *Experiment execution.*

M. B. Wheeler: *Experiment execution.*

T. Wheeler: *Experiment execution.*

C. Wibisono: *Experiment execution.*

M. Wiedeking: *Experiment execution and manuscript revision.*

J. A. Winger: *Experiment execution and manuscript revision.*

Z. Xu: *Experiment execution.*

Y. Zhu: *Experiment execution.*

Competing interests

The authors declare no competing interests.

Additional information

Correspondence and materials requests should be addressed to T. Gaballah (tawfik-gaballah@gmail.com).

Extended data figures and tables

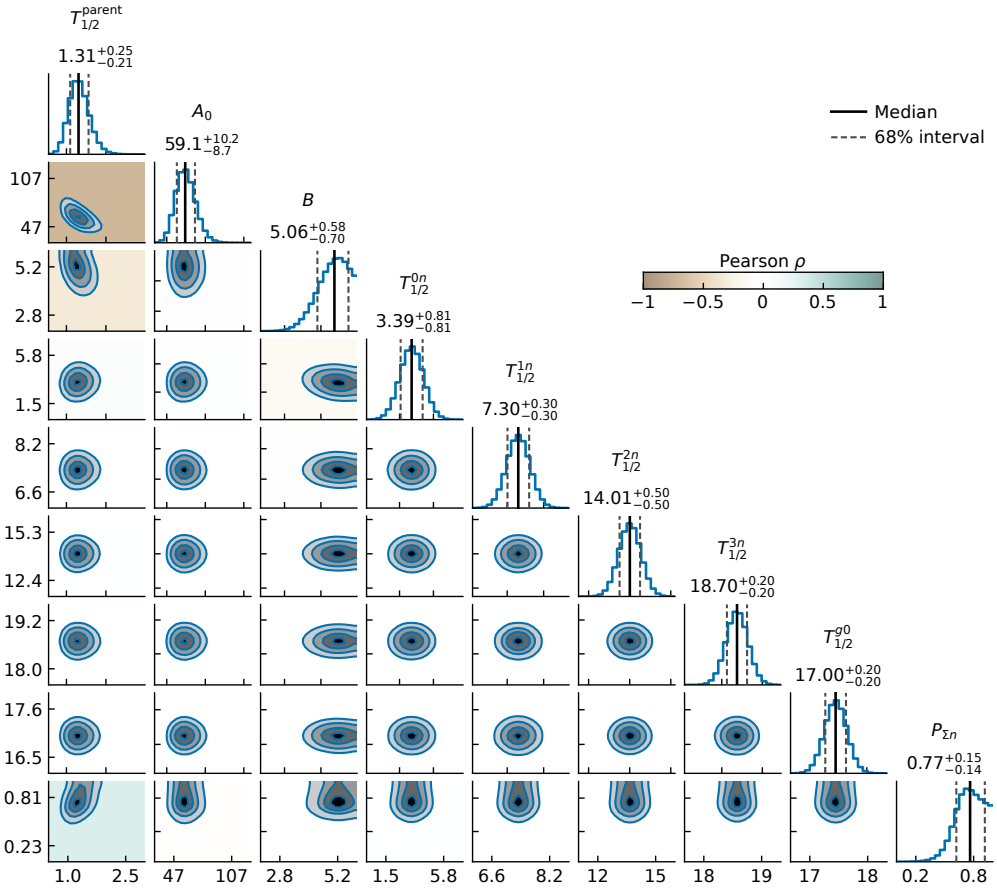

Extended Data Fig. 1 Posterior marginals and correlations for ^{31}F. The corner plot shows 240,000 retained posterior draws. Parameters are the parent half-life $T_{1/2}^{\text{parent}}$, initial activity A_0, constant background B, daughter half-lives $T_{1/2}^{xn}$ (x = 0–3), the $\beta 0n$ granddaughter half-life $T_{1/2}^{g0}$, and the total neutron-emission probability $P_{\Sigma n} = 1 - P_{0n}$. Half-lives are given in ms, A_0 and B in counts per ms, and $P_{\Sigma n}$ is dimensionless. Diagonal panels show the one-dimensional marginal posterior distributions. The solid vertical line marks the median and the dashed lines mark the 16th and 84th percentiles; the median with its central 68% credible interval is given above each marginal distribution. Off-diagonal panels show the pairwise joint posterior distributions as nested density contours corresponding to the 0.5, 1, 1.5 and 2σ two-dimensional credible regions. The background shading indicates the Pearson correlation coefficient ρ for each parameter pair, with the color gradient representing the magnitude of the correlation.

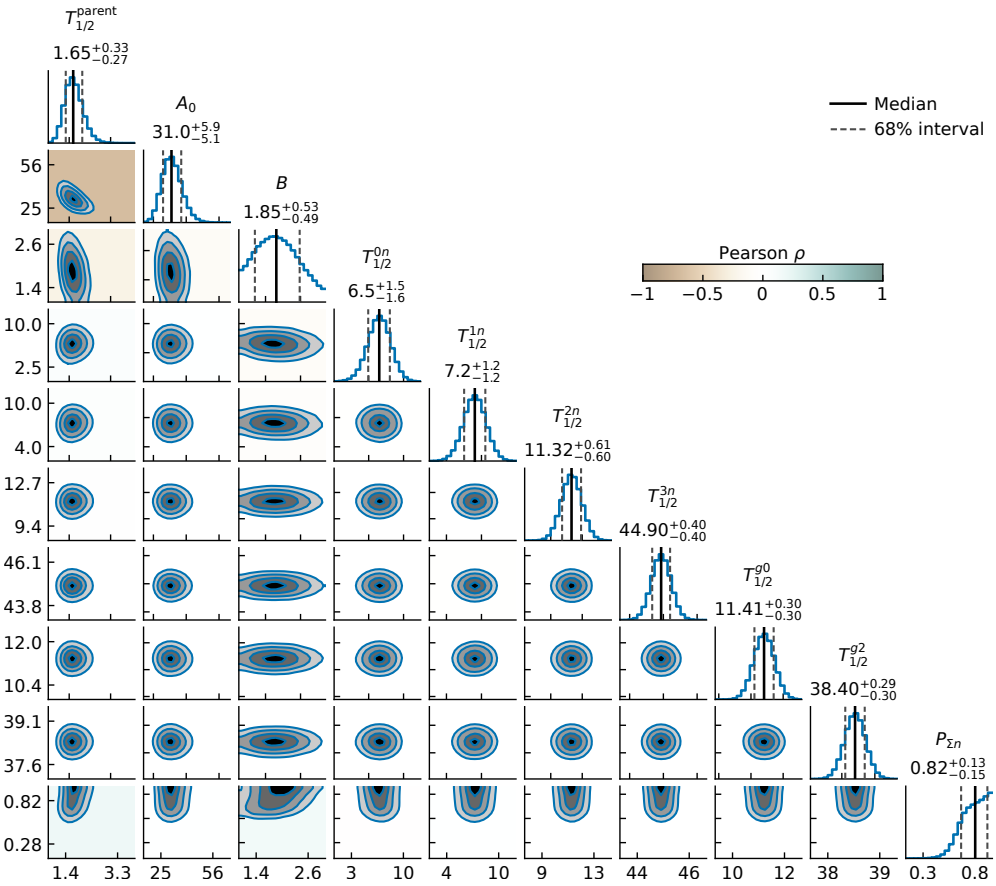

Extended Data Fig. 2 Posterior marginals and correlations for ^{37}Na. The corner plot contains 240,000 retained posterior draws. Parameters are the parent half-life $T_{1/2}^{\mathrm{parent}}$, initial activity A_0, constant background B, daughter half-lives $T_{1/2}^{xn}$ ($x = 0$–3), the $\beta 0n$ and $\beta 2n$ granddaughter half-lives $T_{1/2}^{g0}$ and $T_{1/2}^{g2}$, respectively, and the total neutron-emission probability $P_{\Sigma n} = 1 - P_{0n}$. Half-lives are given in ms, A_0 and B in counts per ms, and $P_{\Sigma n}$ is dimensionless. Diagonal panels show the one-dimensional marginal posterior distributions, with the median indicated by a solid line and the 16th and 84th percentiles by dashed lines; the median with its central 68% credible interval is given above each marginal distribution. Off-diagonal panels show the pairwise joint posterior distributions as nested density contours corresponding to the 0.5, 1, 1.5 and 2σ two-dimensional credible regions. The background shading indicates the Pearson correlation coefficient ρ for each parameter pair, with the color gradient representing the correlation magnitude.

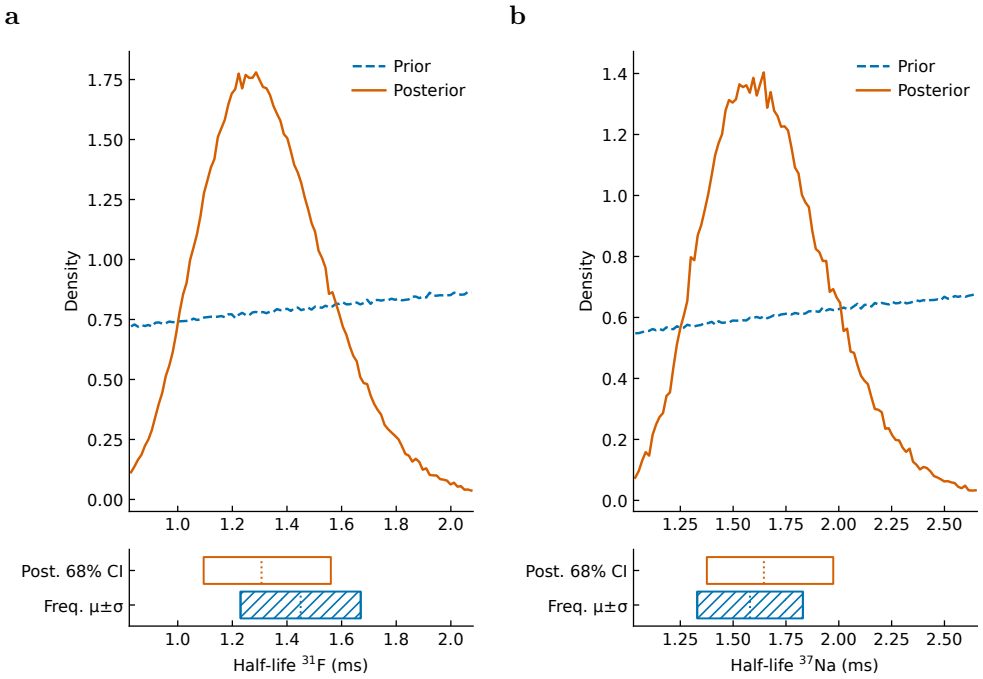

Extended Data Fig. 3 Prior and posterior parent half-life distributions. Bayesian prior and posterior distributions for ^{31}F (**a**) and ^{37}Na (**b**). To resolve the posterior distributions, each panel is restricted to the 0.5th–99.5th percentiles of the posterior, and the displayed curves are normalized within this plotted interval. The lower bars compare the posterior median and central 68% credible interval, bounded by the 16th and 84th percentiles, with the frequentist estimate and its one-standard-deviation interval.

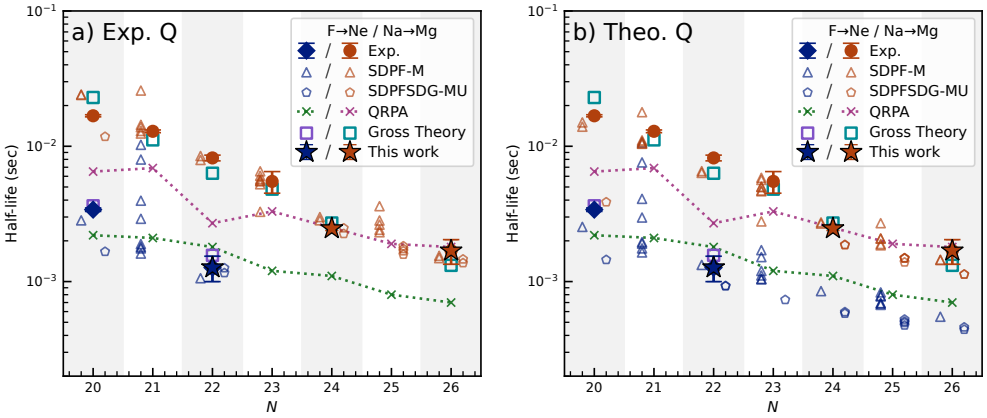

Extended Data Fig. 4 Half-life systematics with two shell-model energy prescriptions. Measured half-lives of neutron-rich F and Na isotopes are compared with theoretical predictions. Shell-model predictions use adopted mass-evaluation Q_β values in **a** and shell-model Q_β values in **b**. SDPF-M and SDPFSDG-MU predictions are denoted by triangles and pentagons; multiple open symbols show alternative candidate ground-state spin-parity assignments. FRDM+QRPA predictions[31] (crosses and dotted lines) and JAEA Gross-theory predictions[33] (open squares) retain their respective global-model mass prescriptions in both panels. Filled diamonds and circles denote experimental F and Na values, respectively; stars mark the present ^{31}F, ^{37}Na and ^{35}Na results. Other experimental values are from NUBASE2020[32] and Ref.[24].

Rank	Nucleus	Z	N	Half-life (ms)	Q_{β^-} (MeV)	Half-life source
1	^{31}**F**	9	22	$\mathbf{1.31}^{+0.25}_{-0.21}$	$(25.66 \pm 0.60)^{\#}$	This work
2	^{37}**Na**	11	26	$\mathbf{1.65}^{+0.33}_{-0.27}$	$(24.92 \pm 0.98)^{\#}$	This work
3	^{35}Na	11	24	$2.4 \pm 0.3 \pm 0.2$	$(22.19 \pm 0.72)^{\#}$	Crawford et al.[24]
4	^{61}Sc	21	40	$2.8^{+2.6}_{-2.0}$	$(16.87 \pm 0.67)^{\#}$	Ong et al.[45]
5	^{19}B	5	14	2.92 ± 0.13	27.36 ± 0.53	NUBASE2020[32]
6	^{38}Mg	12	26	$3.1 \pm 0.4 \pm 0.2$	$(17.60 \pm 0.53)^{\#}$	Crawford et al.[24]
7	^{29}F	9	20	$3.4 \pm 0.4 \pm 0.1$	21.75 ± 0.55	Crawford et al.[24]
7	^{31}Ne†	10	21	3.4 ± 0.8	18.94 ± 0.27	NUBASE2020[32]
9	^{41}Al	13	28	$3.5 \pm 0.8 \pm 0.4$	$(21.39 \pm 0.50)^{\#}$	Crawford et al.[24]
10	^{63}Ti	22	41	$3.6^{+5.1}_{-2.6}$	$(15.88 \pm 0.61)^{\#}$	Ong et al.[45]

Extended Data Table 1 Ten shortest directly measured nuclear β^--decay half-lives. Equal central values share a rank. Where two symmetric half-life uncertainties are given, they are statistical and systematic, respectively. Half-life uncertainties otherwise follow the cited source; those for the present measurements are central 68% credible intervals. Ground-state-to-ground-state Q_{β^-} values and their 1σ uncertainties are from AME2020[27]; # denotes values based at least partly on extrapolated masses. †The ^{31}Ne half-life was extracted from a β-decay curve but remains tentative in the current evaluation[46]. The compilation uses NUBASE2020 with the updates specified in Methods, including the replacement of the older ^{35}Na result. Overlapping uncertainties preclude interpreting the rank as a statistically resolved ordering.

a, ^{31}F

Parameter	Mean	s.d.
$T_{1/2}^{\mathrm{par}}$ (ms)	1.33	0.24
A_0 (counts per ms)	59.9	9.63
B (counts per ms)	4.99	0.62
$T_{1/2}(0n)$ (ms)	3.39	0.81
$T_{1/2}(1n)$ (ms)	7.30	0.30
$T_{1/2}(2n)$ (ms)	14.0	0.50
$T_{1/2}(3n)$ (ms)	18.7	0.20
$T_{g,0}$ (ms)	17.0	0.20
P_{0n}	0.23	0.14
P_{1n}	0.24	0.14
P_{2n}	0.26	0.14
P_{3n}	0.27	0.14
$P_{\Sigma n}$	0.77	0.14

b, ^{37}Na

Parameter	Mean	s.d.
$T_{1/2}^{\mathrm{par}}$ (ms)	1.67	0.31
A_0 (counts per ms)	31.4	5.66
B (counts per ms)	1.87	0.47
$T_{1/2}(0n)$ (ms)	6.49	1.58
$T_{1/2}(1n)$ (ms)	7.23	1.22
$T_{1/2}(2n)$ (ms)	11.3	0.60
$T_{1/2}(3n)$ (ms)	44.9	0.40
$T_{g,0}$ (ms)	11.4	0.30
$T_{g,2}$ (ms)	38.4	0.30
P_{0n}	0.19	0.13
P_{1n}	0.23	0.14
P_{2n}	0.25	0.14
P_{3n}	0.32	0.15
$P_{\Sigma n}$	0.81	0.13

Extended Data Table 2 Posterior parameter summaries. a,b, Posterior means and standard deviations from the Bayesian inference for ^{31}F (**a**) and ^{37}Na (**b**), each from 240,000 posterior draws. Parameters are the parent half-life $T_{1/2}^{\mathrm{par}}$, initial activity A_0, constant background B, daughter half-lives $T_{1/2}(xn)$, active granddaughter half-lives $T_{g,x}$, neutron-emission probabilities P_{xn} $(x = 0, 1, 2, 3)$, and total neutron-emission probability $P_{\Sigma n} = 1 - P_{0n}$.

Supplementary Files

This is a list of supplementary files associated with this preprint. Click to download.

- f31Tparentpriorposteriornature.pdf
- halflifeplotFtoNeNatoMg.pdf
- na37Tparentpriorposteriornature.pdf
- 37Naposteriorcorrelations.pdf
- 31Fposteriorcorrelations.pdf